Finite-Element Analysis of Electrical Machines for Sensorless Drives with High Frequency Signal Injection

Luigi Alberti, *Member, IEEE,* Nicola Bianchi, *Senior Member, IEEE*
Mattia Morandin, *Student Member, IEEE* and Johan Gyselinck

***Abstract*—A challenge during the design process of an electrical machine is the characterization of the various parameters in a computational time as short as possible. Frequently it is required the computation of the electrical machine parameters which are necessary for the tuning of the drive control algorithm. This paper deals with a strategy to compute the high frequency signal injection response of a sensorless controlled electrical machine. It allows to determine the self-sensing capability of the machine directly during the design process. Such a capability can be defined in any given operating point, for example along the Maximum Torque Per Amps trajectory. Then, also the high frequency machine parameters can be computed.**

In addition, the strategy proposed here requires a very short computational time to get such a data. After a magnetostatic field analysis, carried out so as to get the torque for a given current, the flux density distribution is stored and the differential reluctivity tensor is evaluated in each element of the mesh. Then, a time-harmonic analysis is carried out in a linearized structure so as to compute the d-q parameters at the injection frequency.

In order to validate the proposed procedure, experimental results on different machine type are included in the paper. This allows to prove the reliability of the procedure as a valued tool for the characterization of the machine.

I. Introduction

Sensorless techniques for the detection of the rotor position have been proposed some years ago in order to remove the position sensor in the electrical drive. This allows to reduce the cost, to reduce the time to initialize the system and to increase the fault-tolerant capability of the drive. Such techniques are generally based on the magnetic saliency of the rotor. They have been proposed for induction motors [1], [2], or induction generators [3], [4], as well as for synchronous machines of different type [5], [6]. Sometimes, the magnetic saliency is artificially added to the rotor in order to increase the self-sensing capability [7]. In addition, there is a growing interest to apply these techniques in various applications, such as aerospace, industrial drives, automotive, etc.

In the past literature, it has been highlighted that satisfactory performance is achieved by means of a proper combination of both sensorless control algorithms and electrical machine geometry [8], [9]. In other words, a proper electrical machine structure is necessary in order to guarantee an adequate self-sensing capability in the desired operating region.

Various models have been proposed taking into account the slot effects and the machine non linearities [10]–[13]. It was highlighted that an accurate analysis is mandatory to evaluate the self-sensing capability of the machine. This is particularly important during the design process when various machine geometries have to be compared [14], [15].

Further, additional aspects, as eddy current losses in permanent magnets, eddy currents and hysteresis of lamination, have to be included in the analysis. It has been also shown that eddy currents have been exploited usefully for the rotor angle detection. In some cases, the combination of different high frequency responses of the machine allows an improvement of its self-sensing capability (i.e. resistive saliency versus magnetic saliency) [16], [17].

However, it is not always easy to consider all these aspects in the machine analysis. Various simulation strategies are adopted to evaluate the self-sensing capability of the machine. Anyway, a large amount of computation time is often required for modeling the machine. For instance, time stepping analysis is proposed in [18] to simulate properly the machine under the actual supply conditions including high frequency injection signal. As recognized by the authors, this requires a huge computational time which makes hard to adopt such an analysis in office-routine computation. On the other hand, in magnetostatic simulations time-dependent phenomena such as eddy currents are not considered.

This paper presents a strategy to compute the high frequency signal injection response of an electrical machine adopted in a sensorless electric drive. The aim is to obtain the electrical machine parameters necessary for the drive control as quickly as possible. In particular, the proposed strategy is focused on how to assess the self-sensing capability of the machine during the design process. Such a capability is computed in any given operating point. In addition, the computation time required to get such an information is very short. After a magnetostatic field analysis, carried out so as to simulate the actual working point, the flux density distribution is stored and the differential reluctivity tensor is evaluated in each element of the mesh. This correspond to freeze the permeability in each mesh element. Then, a time-harmonic analysis is carried out in a linearized structure so as to compute the current response to the high frequency injection signal, or, alternatively, to computed the d-q high frequency parameters. In order

Luigi Alberti is with the Faculty of Science and Technology Free University of Bozen, Bozen, Italy, luigi.alberti@unibz.it. Nicola Bianchi and Mattia Morandin are with the Department of Industrial Engineering, University of Padova, Padova, Italy, nicola.bianchi@unipd.it. Johan Gyselinck is with the Dept. of Bio-Electro-Mechanical Systems Université Libre de Bruxelles, Bruxelles, Belgium, johan.gyselinck@ulb.ac.be.

to validate the proposed procedure, experimental results are included in the paper. Instead of given a full characterization of only one machine, three machines of different type are considered and the more particular aspects of each are presented. In this way the generality and the reliability of the proposed procedure can be validated. Nevertheless each machine can be fully characterized by the proposed procedure.

II. The d-q model of synchronous machines

As far as the magnetic model of the electrical machine is concerned, the classical d-q model in the rotor reference frame is used. The stator currents are assumed as state variables. The d- and the q-axis flux linkages depend on both currents due to cross saturation, i.e. they can be written as $\lambda_{sd}(i_{sd}, i_{sq})$ and $\lambda_{sq}(i_{sd}, i_{sq})$. Since the considered control technique is typically applied at zero or quasi-zero speed, the rotor speed ω_m^e is assumed to be zero.

Therefore, the voltage equations in the rotor reference frame are:

$$\begin{aligned} v_{sd} &= R_s i_{sd} + \frac{d\lambda_{sd}}{dt} \\ v_{sq} &= R_s i_{sq} + \frac{d\lambda_{sq}}{dt} \end{aligned} \tag{1}$$

Where R_s is the stator phase-resistance.

A. Small-signal model

When the machine is working at steady state, it is possible to describe the small variations around the working point adopting a small-signal model.

Let the working point of the motor be defined by the steady state currents (I_{sd0}, I_{sq0}), i.e. by the selected state variables. Then, δi_{sd} and δi_{sq} are small variations of the d- and q-axis currents around such a working point, so that the total current results as:

$$\begin{aligned} i_{sd} &= I_{sd0} + \delta i_{sd} \\ i_{sq} &= I_{sq0} + \delta i_{sq} \end{aligned} \tag{2}$$

Then, the flux linkages are expressed as:

$$\begin{aligned} \lambda_{sd}(i_{sd}, i_{sq}) &= \Lambda_{sd0} + \delta\lambda_{sd} \\ \lambda_{sq}(i_{sd}, i_{sq}) &= \Lambda_{sq0} + \delta\lambda_{sq} \end{aligned} \tag{3}$$

where Λ_{sd0} and Λ_{sq0} are the steady state flux linkages in the considered working point and the small variations are given by:

$$\begin{aligned} \delta\lambda_{sd} &= \frac{\partial\lambda_{sd}}{\partial i_{sd}}\delta i_{sd} + \frac{\partial\lambda_{sd}}{\partial i_{sq}}\delta i_{sq} \\ \delta\lambda_{sq} &= \frac{\partial\lambda_{sq}}{\partial i_{sd}}\delta i_{sd} + \frac{\partial\lambda_{sq}}{\partial i_{sq}}\delta i_{sq} \end{aligned} \tag{4}$$

or

$$\begin{aligned} \delta\lambda_{sd} &= l_{dd}\ \delta i_{sd} + l_{dq}\ \delta i_{sq} \\ \delta\lambda_{sq} &= l_{qd}\ \delta i_{sd} + l_{qq}\ \delta i_{sq} \end{aligned} \tag{5}$$

where l_{dd}, l_{qq}, l_{dq} and l_{qd} are the differential inductances defined as the partial derivative of the flux linkages evaluated in the considered working point. Therefore, they are a function of the working point (I_{sd0}, I_{sq0}). Thanks to the reciprocity property, and neglecting hysteretic phenomena, the differential inductances l_{dq} and l_{qd} between the two axes are equal [19].

Similarly, the voltage equations for small variations around the working point can be considered as:

$$\begin{aligned} v_{sd} &= V_{sd0} + \delta v_{sd} \\ v_{sq} &= V_{sq0} + \delta v_{sq} \end{aligned} \tag{6}$$

where V_{sd0} and V_{sq0} are the steady state values and δv_{sd} and δv_{sq} are the small variations around the working point.

Finally neglecting eddy currents in the rotor, it is

$$\begin{aligned} \delta v_{sd} &= R_s\delta i_{sd} + l_{dd}\ \frac{d}{dt}\delta i_{sd} + l_{dq}\ \frac{d}{dt}\delta i_{sq} \\ \delta v_{sq} &= R_s\delta i_{sq} + l_{qd}\ \frac{d}{dt}\delta i_{sd} + l_{qq}\ \frac{d}{dt}\delta i_{sq} \end{aligned} \tag{7}$$

The last equation can be used to computed the stator current response under a particular voltage excitation. As well known, the current response contains information about the rotor position (contained in the magnetic parameters l_{dd}, l_{qq}, and l_{dq}) and can be processed to estimate the actual rotor position [1].

B. Sinusoidal variation

The model described by (7) is valid whatever time variations are considered. For high frequency signal injections, particularly interesting are sinusoidal variations around the working point. In such a case, it is possible to adopt the complex notation for the time dependent quantities and (7) can be rewritten as:

$$\begin{aligned} \overline{v}_{sd} &= R_s\ \overline{\imath}_{sd} + j\omega_{hf} l_{dd}\ \overline{\imath}_{sd} + j\omega_{hf} l_{dq}\ \overline{\imath}_{sq} \\ \overline{v}_{sq} &= R_s\ \overline{\imath}_{sq} + j\omega_{hf} l_{qd}\ \overline{\imath}_{sd} + j\omega_{hf} l_{qq}\ \overline{\imath}_{sq} \end{aligned} \tag{8}$$

where overlined symbols are used for complex quantities and ω_{hf} is the angular frequency of the injected carrier signal.

C. High frequency rotor losses

The model described above can be generalized also to take into account the eddy current phenomenon in the conductive parts due to the injected field. Such currents can decrease the machine performance [20], [21]. In other cases, such eddy currents can be exploited in order to track a resistive saliency instead of a magnetic saliency [16], [17].

In order to consider the presence of the rotor eddy currents, (8) can be generalized as:

$$\begin{aligned} \overline{v}_{sd} &= R_s\ \overline{\imath}_{sd} + \dot{z}_{dd}\ \overline{\imath}_{sd} + \dot{z}_{dq}\ \overline{\imath}_{sq} \\ \overline{v}_{sq} &= R_s\ \overline{\imath}_{sq} + \dot{z}_{qd}\ \overline{\imath}_{sd} + \dot{z}_{qq}\ \overline{\imath}_{sq} \end{aligned} \tag{9}$$

since the impedances $\dot{z}_{dd}$, $\dot{z}_{qq}$, $\dot{z}_{dq}$, and $\dot{z}_{qd}$ take into account both the resistive and inductive part of the injected fields along the d- and q-axis.

Considering the model described in (9), both the magnetic and resistive saliency of the electrical machine are modeled. Moreover, a better estimation of the machine self-sensing capability is obtained since both the cross saturation and the eddy currents are considered. Finally, the Joule losses associated to the eddy currents due to the injected field are directly evaluated.

III. Finite element simulations

The machine response to the high frequency injection signal is computed by means of suitable finite element (FE) analysis, so as to evaluate its self-sensing capability in various loading conditions. The simulations are carried out adopting a small-signal model of the machine so that it is possible to consider time-dependent effects as eddy currents induced by the injected signal.

This is achieved using the frozen permeability method as described in the following. Such a technique has been used in the past for different purposes: to model the electrical machine under saturated conditions [22], to weigh the flux linkage contributions to the average torque [23], and to segregate the torque components [24]. In all these works, only magnetostatic analysis has been adopted for their purpose, since the high frequency analysis was not considered. The purpose of such study is different: to compute the magnetic quantities that are not the steady state quantities (required for instance to compute the torque). In this work, the frozen magnetic permeability is considered as a tensor, taking into account the direction of the flux density. In the FE implementation it is more convenient to use the reluctivity ν which is the inverse of permeability μ. So that, in the following the reluctivity tensor will be considered.

Applications of the procedure to compute the current response and the high frequency parameters is presented in the next Section. For the finite element simulations, the GetDP package has been used [25]. The proposed simulation strategy is composed of three main steps:

(i) polarization simulation;
a nonlinear magnetostatic current driven simulation is carried out in the working point (I_{sd0}, I_{sq0}). This simulation allows to take into account carefully the non linear characteristic of the iron and all the excitation of the machine are included, i.e. winding currents and PMs. At the end of this simulation, the flux density distribution $\mathbf{B}_0 = (B_{0x}, B_{0y})$ in each element of the mesh is stored.

(ii) Differential reluctivity tensor construction;
the stored flux density distribution $\mathbf{B}_0$ is used to compute the differential reluctivity tensor that is required for the small variation simulation. A tensor is considered to represent the iron differential reluctivity since the small-signal variation of the magnetic field is, in general, not aligned with the main field [26]. The differential reluctivity tensor is defined element wise. It describes completely the polarization state of the machine. Adopting 2D Cartesian coordinates, the differential reluctivity tensor is written as:

$$\begin{bmatrix} \frac{\partial h_x}{\partial b_x} & \frac{\partial h_x}{\partial b_y} \\ \frac{\partial h_y}{\partial b_x} & \frac{\partial h_y}{\partial b_y} \end{bmatrix} = \nu(\mathbf{B}_0) \begin{bmatrix} 1 & 0 \\ 0 & 1 \end{bmatrix} + 2 \left. \frac{d\nu}{dB^2} \right|_{B_0} \begin{bmatrix} bb \end{bmatrix} \tag{10}$$

where

$$\begin{bmatrix} bb \end{bmatrix} = \begin{bmatrix} \delta b_x \delta b_x & \delta b_x \delta b_y \\ \delta b_y \delta b_x & \delta b_y \delta b_y \end{bmatrix} \tag{11}$$

The scalar reluctivity $\nu(\mathbf{B}_0)$ is a single-valued function of the stored flux density distribution $\mathbf{B}_0$. The derivative $d\nu/dB^2$ is the derivative of the differential reluctivity respect to the flux density square, again evaluated at the stored value $\mathbf{B}_0$. δb_x and δb_y are the small-signal variations of the flux density. Due to the presence of $\mathbf{B}_0$ in (10), the differential reluctivity tensor depends on the actual working point (I_{sd0}, I_{sq0}).

(iii) Small variation simulation;
At last, a time-harmonic voltage driven simulation in the frequency domain is carried out, imposing the frequency of the injected signal. The analysis is carried out at standstill, i.e. with electrical speed ω_m^e=0. In the iron, the differential reluctivity tensor is computed by (10). This simulation step represents the small variation around the working point, so that there is only the injection signal as excitation during the simulation, i.e. the PMs are not active. In such a time-harmonic simulation, sinusoidal quantities are assumed so that complex voltages, flux linkages and currents are considered. The voltages at the motor terminals are imposed and the current response is computed directly in the FE simulation including circuit equations in the system. The machine model is described by (9).

(iv) High frequency parameters;
Alternatively, the small-signal simulation can be adopted to compute the high frequency parameters of the machine as:

$$\begin{aligned} \dot{z}_{dd} &= \left. \frac{\overline{v}_{sd} - R_s\ \overline{\imath}_{sd}}{\overline{\imath}_{sd}} \right|_{\overline{\imath}_{sq}=0} & \dot{z}_{dq} &= \left. \frac{\overline{v}_{sd}}{\overline{\imath}_{sq}} \right|_{\overline{\imath}_{sd}=0} \\ \dot{z}_{qq} &= \left. \frac{\overline{v}_{sq} - R_s\ \overline{\imath}_{sq}}{\overline{\imath}_{sq}} \right|_{\overline{\imath}_{sd}=0} & \dot{z}_{qd} &= \left. \frac{\overline{v}_{sq}}{\overline{\imath}_{sd}} \right|_{\overline{\imath}_{sq}=0} \end{aligned} \tag{12}$$

In order to use (12) two current driven simulations are required, supplying each axis separately. In this case the voltages at the machine terminals are computed from the circuit equations included in the system.

Repeating the simulation steps described above in different working points, it is possible to characterize the machine in a whole operating region. It is worth noticing that once the polarization simulation has been carried out (step *i*) and the reluctivity tensor constructed (step *ii*), more than one small variation simulation (step *iii*) can be executed. This is useful, for example, when the impact of the injection frequency on the self-sensing capability is under investigation. The main computational time is required for the polarization simulation (step *i*) which is nonlinear. The small variation simulation (step *iii*) is linear so that it is solved very fast. Therefore, the proposed strategy is very efficient for the investigation of self-sensing capability.

A. Time-domain simulations

The self-sensing capability of a machine can also be investigated adopting non-linear finite element simulations in the time domain. In this case, the machine is supplied with the actual voltages that includes both the steady state voltages and the injected voltage signals. The current responses are directly computed in the time domain.

However, in this case the computational time is much larger since the time has to be discretized on the basis of the injection frequency which is usually quite higher than the main supply frequency. Such a simulation strategy is considered hereafter to compare the results of the small-signal simulation strategy presented above as well as the experimental results.

IV. Experimental validation

The simulation strategy described in the previous Section is adopted to compute the current response and the high frequency parameters of different machine type. An interior permanent magnet (IPM) machine, an inset PM machine and a ringed-pole PM machine are considered in the following. Such machines are characterized by different types of saliency, so as to prove the generality of the proposed strategy.

The machine shaft is locked so that the tests are carried out at zero speed. The actual rotor position, measured by means of a position sensor, is used in the simulations for the comparison.

The adopted control scheme is shown in Fig. 1. A fast-prototyping system is adopted to control the inverter. The machine is controlled by a voltage-source inverter which imposes high frequency voltage signals superimposed to different steady state voltages. Both currents and voltages are measured.

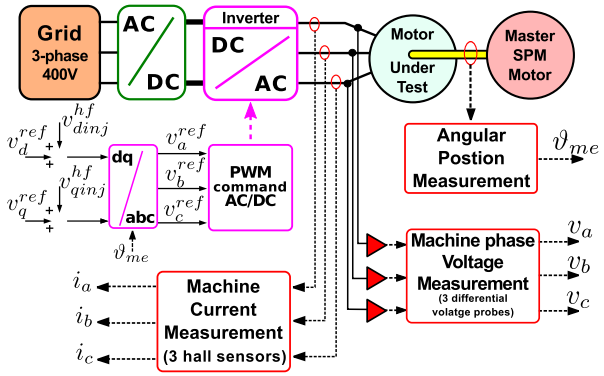

Fig. 1. Control scheme adopted in the experimental test

A. Interior permanent magnet machine

Fig. 2 shows a sketch of the geometry of the IPM prototype. It is a 12-slot 8-pole machine with three flux barriers per pole. Details of such a machine and all its data can be found in [27].

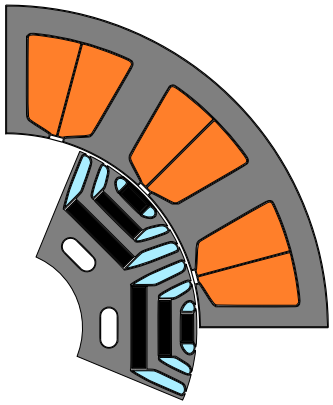

Fig. 2. FE model of the 12-slot 8-pole interior permanent magnet prototype (only 2-pole section is shown)

Such a kind of machine is characterized by a strong non-linear behavior. Fig. 3 shows the d- and q-axis flux linkages in various operating points. The cross saturation effect is clearly visible.

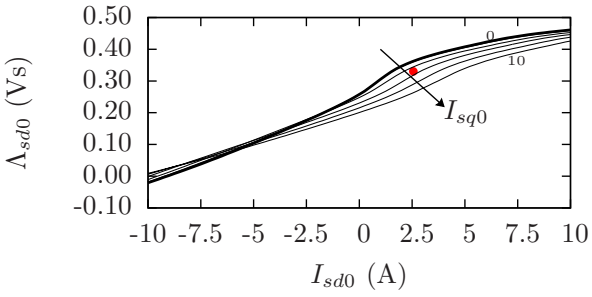

(a) d-axis flux linkage

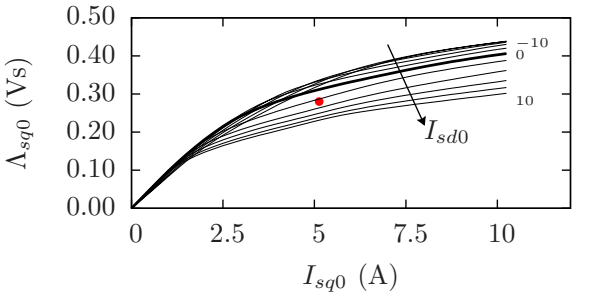

(b) q-axis flux linkage

Fig. 3. Flux linkages of the IPM prototype computed in different working points

The machine is tested in the point highlighted by red dots in Fig. 3. A positive d-axis current, i.e. magnetizing current, is supplied. A pulsating voltage of 60 V (peak value) has been imposed on the d-axis. The selected injection frequency is 250 Hz. Fig. 4 shows the computed and measured current response. For a better comparison, the a-, b- and c-phase currents (directly measured) are shown. A satisfactory agreement is achieved between predicted and measured currents.

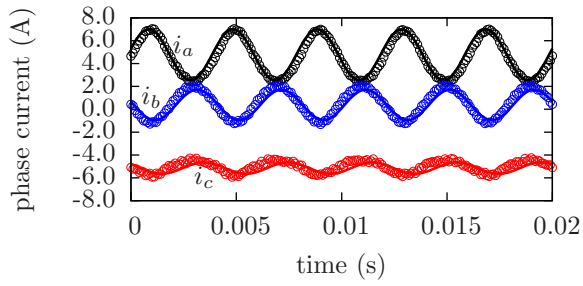

Fig. 4. Computed (solid line) and measured (circles) current response of the IPM prototype

B. Inset permanent magnet machine

In this Section, an inset PM machine is considered. Such a kind of machine is similar to the commonly used surface mounted PM machine, but it is characterized by iron teeth between each couple of adjacent PMs. Therefore, the inset PM motor exhibits a rotor anisotropy, which can be exploited to detect the rotor position. An overview

about the advantages in adopting such a rotor structure is presented in [9].

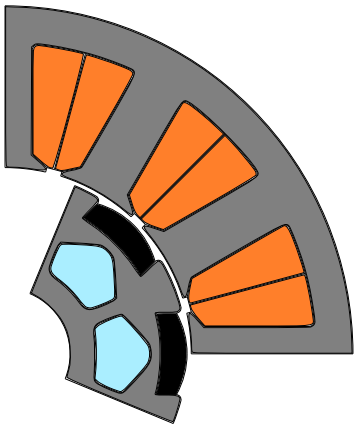

Fig. 5. FE model of the 12-slot 8-pole inset permanent magnet prototype (one fourth of machine is reported)

Fig. 5 shows a sketch of the geometry of the considered prototype. It is a fractional-slot machine with 12 slots and 8 poles. Fig. 6 shows the flux linkages of both the d- and q-axis. As can be noted, the cross saturation effect is again present, especially at higher currents.

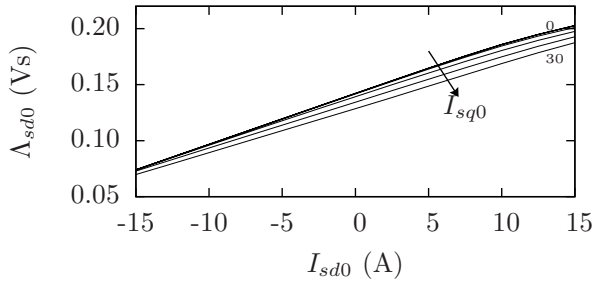

(a) d-axis flux linkage

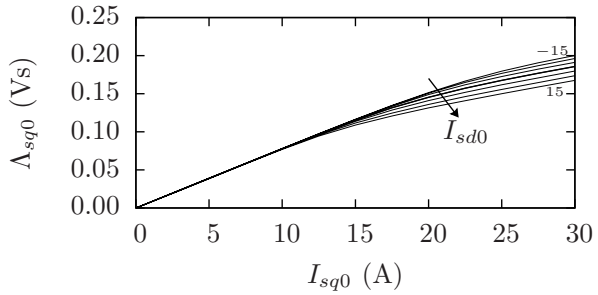

(b) q-axis flux linkage

Fig. 6. Flux linkages of the inset PM prototype computed in different working points

The high frequency current response is computed by means of the simulation strategy described in Section III. Fig. 7 shows the comparison between the computed and measured currents. Both pulsating and rotating voltage injection are applied to the inset prototype. The voltage amplitude is 30 V in both cases and the frequency is equal to 500 Hz. Figs. 7(a) and 7(b) show the current responses for the pulsating and the rotating injection, respectively. A good agreement can be noted between predictions and measurements.

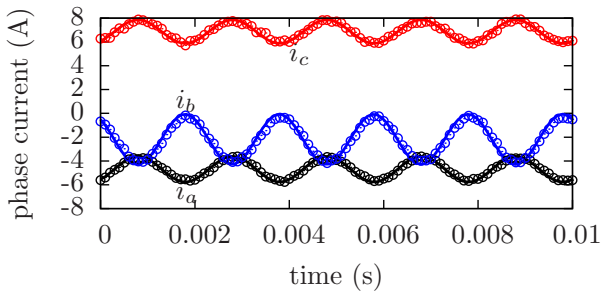

(a) 30 V pulsating voltage at 500 Hz

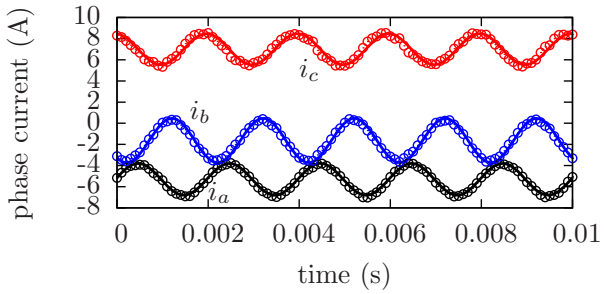

(b) 30 V rotating voltage at 500 Hz

Fig. 7. Computed (solid line) and measured (circles) current response of the inset PM prototype

The high frequency parameters are also predicted. For each working point, two current-driven simulations are carried out and then the parameters are computed adopting (12). In such a machine, the real part of the high frequency parameters is very small with respect to the imaginary part, i.e. the eddy current effects are negligible in comparison to the magnetic saliency. Therefore, only the differential inductances are shown in Fig. 8. As expected, the q-axis inductance is higher than the d-axis inductance. The cross saturation inductance l_{dq} is different from zero only with a q-axis current higher than 12 A. The curves shown in Fig. 8 represent the slopes of the flux linkage characteristics of Fig. 6 as defined by (4).

C. Ringed-pole permanent magnet machine

At last, the ringed-pole PM prototype described in [17] is considered. It is a 27-slot 18-pole outer rotor PM machine. Fig. 9(a) shows a picture of the rotor of the prototype. Fig. 9(b) shows a detail of a pole pairs surrounded by the copper cage. The purpose of such a cage is to modify the HF d-axis magnetic path.

Fig. 10 shows a sketch of the model adopted in the simulations. The static d- and q-axis flux linkages are reported in Fig. 11. The cross-saturation effect exists also in the ringed-pole prototype, even if it is quite low.

Fig. 12 compares the measured currents with the reconstructed high frequency currents, computed by means of the simulation strategy described in Section III. The considered injection supply is a pulsating voltage of 30 V on the d-axis at 500 Hz. A good agreement between predictions and measurements is noted also in this case.

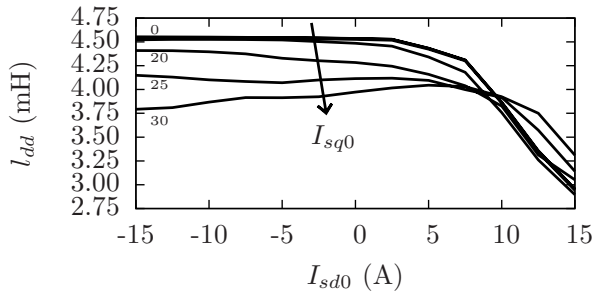

(a) HF d-axis self-inductance

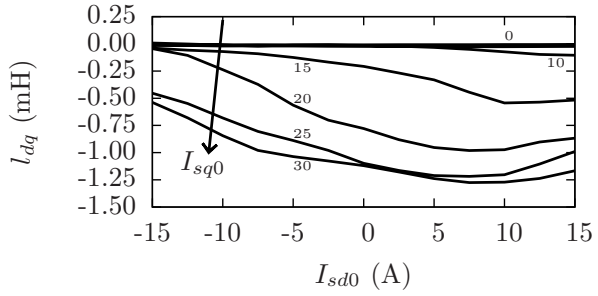

(b) HF cross-saturation inductance

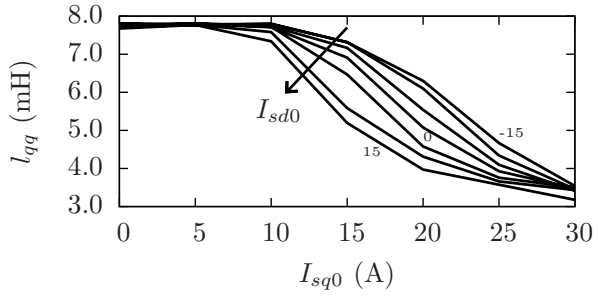

(c) HF q-axis self-inductance

Fig. 8. High frequency computed parameters of the inset PM prototype

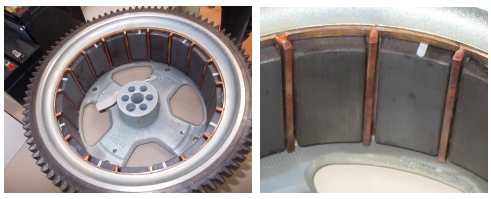

(a) whole rotor (b) particular of the PMs with the copper ring

Fig. 9. A picture of the rotor of the considered ringed-pole permanent magnet prototype

V. Comparison with time-domain FE analysis

As a final validation of the proposed procedure, time-stepping finite element simulations are carried out considering the ringed-pole machine. The same working operations considered in Sec.IV-C is simulated in order to compare the results. The current responses are compared with the experimental measurements in Fig. 13 (the measured values are the same as in Fig. 12). The simulations are voltage driven, so that a transient term is present in the currents, as visible during the first 4 ms in Fig. 13. Experimental currents are compared once the steady state operation is reached.

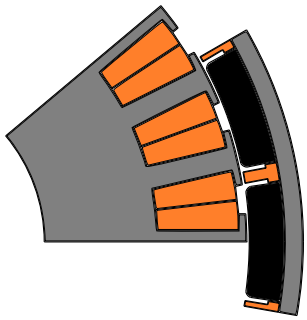

Fig. 10. FE model of the 27-slot 18-pole ringed-pole permanent magnet prototype (only 2-pole section is shown)

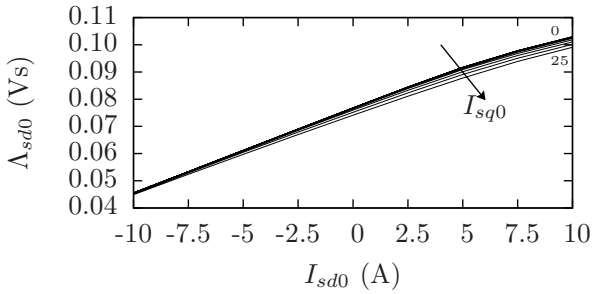

(a) d-axis flux linkage

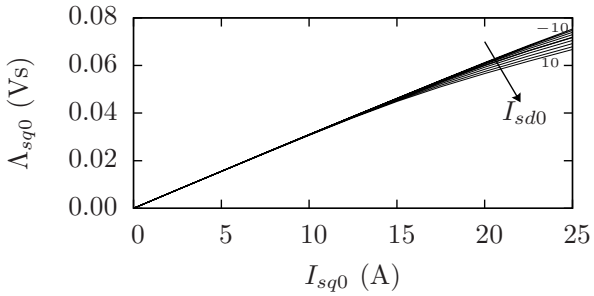

(b) q-axis flux linkage

Fig. 11. Flux linkages of the ringed-pole PM prototype computed in different working points

It is worth noticing that the time domain simulation yields the same current response as the small-signal finite element strategy presented in Section III. The computational time is, however, not comparable since the small-signal simulation strategy is very faster than the time domain simulation. The comparison highlights that adopting the proposed small-signal finite element strategy the same results of the time domain finite element simulations are obtained but in a greatly reduced time, since only two finite element simulations are required.

Finally, the current induced in the rotor ring is computed. Fig. 14(a) shows the current in the ring computed in the time domain simulation. The initial transient is visible in the figure. Also the eddy current losses in the copper ring due to the injected field is computed. They are shown in Fig. 14(b). The losses in the PMs and in the rotor yoke are limited, while the higher amount of losses is found in the ring as expected. The total losses result about 10 W once the steady state is reached. The same rotor losses

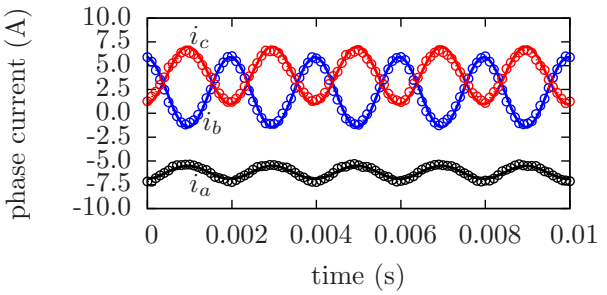

Fig. 12. Computed (solid line) and measured (circles) current response of the ringed-pole PM prototype. Computations by means of small-signal finite element simulations

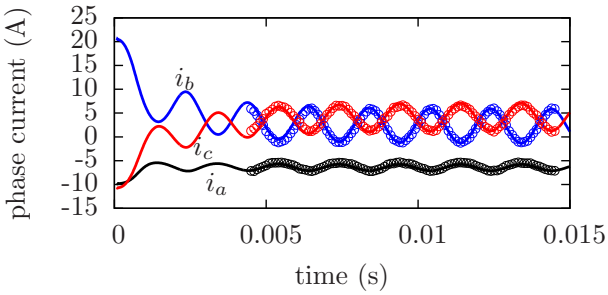

Fig. 13. Computed (solid line) and measured (circles) current response of the ringed-pole PM prototype. Computations by means of time domain finite element simulations

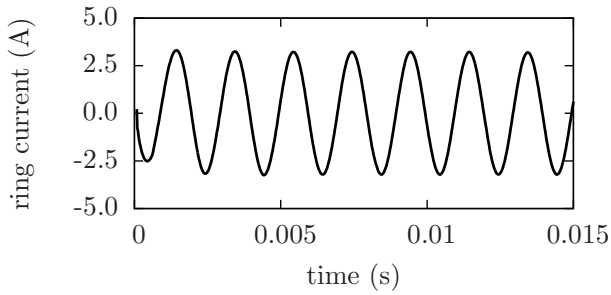

(a) Ring current

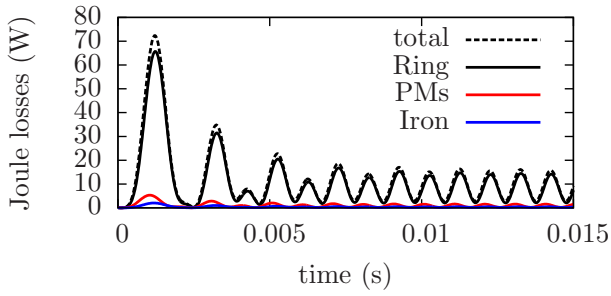

(b) Joule losses in the rotor

Fig. 14. Time domain simulation of the ringed-pole PM prototype, ring current and rotor Joule losses

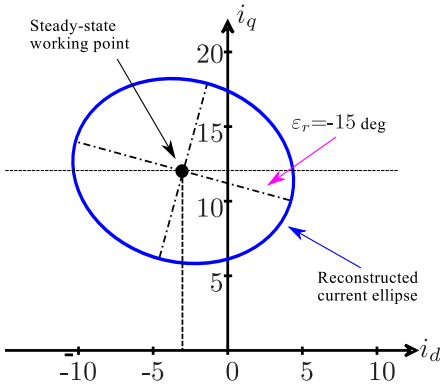

Fig. 15. Reconstructed ellipse in the i_d-i_q plane. Working point is I_{sd0}=-3, I_{sq0}=12. Injected voltage is 60 V rotating at 500 Hz

are estimated by means of the small-signal FE simulation, resulting in 10 W, that is, in agreement with the curve reported in Fig. 14(b). From the same results, the losses are computed as follows in the various machine parts: rotor iron, 0.5 W; PMs, 0.7 W and copper ring, 8.8 W. Further analysis of the ringed-pole machine is described in [28].

VI. Application Example

In this Section an application example of how the proposed strategy can be adopted to estimate the self-sensing capability of a machine is presented.

Once the current response is computed with the proposed procedure as described above, it is possible to reconstruct the current ellipse in the d-q plane in order to to compute the self-sensing capability of the machine. An example of the reconstructed current ellipse is shown in Fig. 15 for the ringed-pole PM machine. The considered working point is I_{sd0}=-3, I_{sq0}=12. A rotating injection voltage of 60 V at 500 Hz has been applied. The magnetic saliency is computed as the ratio between the major and minor axes of the ellipse. In Fig. 15 it is evident the ellipse rotation, i.e. the error angle due to the mutual coupling between the d- and q-axis. In the considered working point such an angle is ε_r=15 electrical degrees.

Repeating the analysis at different frequencies, the machine saliency can be computed as a function of the injection frequency. As described in Section III, the presented strategy is particularly efficient in such a case.

An example of such computation is shown in Fig. 16 (dashed line) where the saliency is reported versus the frequency of the signal injection. Also different working points are considered (no load and maximum torque operations). As expected, increasing the current, i.e. the torque, the saliency decreases. The curves of Fig. 16 can be profitably used to identify the best injection frequency. The saliency variation from no-load to full load is about 5%. The measured saliency at no load for different frequency values (red square) are also reported in Fig. 16. The measured values are in satisfactory agreement with predictions confirming the validity of the proposed strategy.

Fig. 16 shows also the saliency versus the injection frequency for the machine without the ring, i.e. for a pure SPM machine. As expected, the saliency in this case is almost unity at frequencies lower than 1000 Hz. Then, the induced currents in the PMs produce an increase of the saliency. The presented example shows how the proposed strategy can be profitably used to compare the sensorless capability of different machine designs.

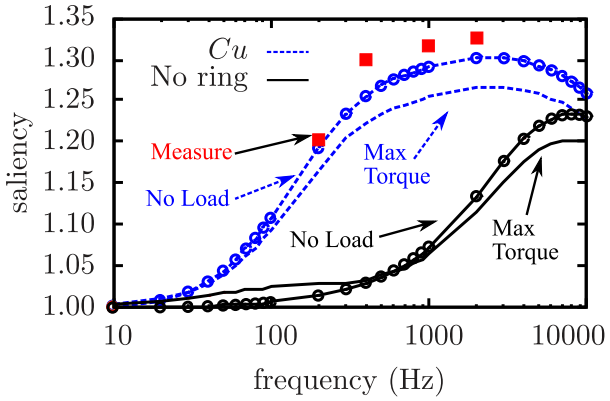

Fig. 16. Computed saliency of the ringed-pole motor with copper ring at different HF injection frequency and working point. Measured values, carried out on a copper ring rotor, are reported with red square for comparison.

VII. Conclusions

A novel simulation strategy is proposed to determine the response of an electrical machine to the high frequency injection signal. This allows to evaluate properly the self-sensing capability of the machine during the design process considering a wide range of operating points. Both non-linearity and parasitic effects are taken into account.

The proposed strategy is very rapid requiring a limited computational time since only one non-linear field solution is necessary for each operating point. It has been applied to analyze various PM machines characterized by saliency of different nature. The comparison between the results of the small-signal analysis with experimental tests confirms the accuracy of the proposed procedure in all cases.

VIII. Acknowledgment

This work was financed by the University of Padova, Padova (Italy) by means of Project CPDA-081750/08 and by the Electric Drives Laboratory (EDLab), Department of Industrial Engineering, University of Padova.

References

[1] M. W. Degner and R. D. Lorenz, "Using multiple saliencies for the estimation of flux, position, and velocity in AC machines," *IEEE Transactions on Industry Applications*, vol. 34, no. 5, pp. 1097–1104, Sep./Oct. 1998.

[2] J. Holtz, "Sensorless position control of induction motors-an emerging technology," *IEEE Transactions on Industrial Electronics*, vol. 45, no. 6, pp. 840–851, Dec. 1998.

[3] G. Iwanski and W. Koczara, "Sensorless Direct Voltage Control of the Stand-alone Slip-ring Induction Generator," *IEEE Transactions on Industrial Electronics*, vol. 54, no. 2, pp. 1237–1239, Apr. 2007.

[4] R. Pena, R. Cerdenas, J. Proboste, G. Asher, and J. Clare, "Sensorless Control of Doubly-fed Induction Generators Using a Rotor-current-based MRAS Observer," *IEEE Transactions on Industrial Electronics*, vol. 55, no. 1, pp. 330–339, Jan. 2008.

[5] A. Consoli, F. Russo, G. Scarcella, and A. Testa, "Low- and zero-speed sensorless control of synchronous reluctance motors," *IEEE Transactions on Industry Applications*, vol. 35, no. 5, pp. 1050 – 1057, sep/oct 1999.

[6] J.-H. Jang, S.-K. Sul, J.-I. Ha, K. Ide, and M. Sawamura, "Sensorless drive of surface-mounted permanent-magnet motor by high-frequency signal injection based on magnetic saliency," *IEEE Transactions on Industry Applications*, vol. 39, no. 4, pp. 1031 – 1039, july-aug. 2003.

[7] J. Cilia, G. M. Asher, K. J. Bradley, and M. Sumner, "Sensorless position detection for vector-controlled induction motor drives using an asymmetric outer-section cage," *IEEE Transactions on Industry Applications*, vol. 33, no. 5, pp. 1162–1169, Sep./Oct. 1997.

[8] N. Bianchi, S. Bolognani, J.-H. Jang, and S.-K. Sul, "Comparison of PM motor structures and sensorless control techniques for zero-speed rotor position detection," *IEEE Transactions on Power Electronics*, vol. 22, no. 6, pp. 2466 –2475, nov. 2007.

[9] N. Bianchi, S. Bolognani, J.-H. Jang, and S.-K. Sul, "Advantages of inset PM machines for zero-speed sensorless position detection," *IEEE Transactions on Industry Applications*, vol. 44, no. 4, pp. 1190 –1198, july-aug. 2008.

[10] A. Ferrah, P. J. Hogben-Laing, K. J. Bradley, G. M. Asher, and M. S. Woolfson, "The effect of rotor design on sensorless speed estimation using rotor slot harmonics identified by adaptive digital filtering using the maximum likelihood approach," in *Record of the Thirty-Second IEEE Industry Applications Annual Meeting Conference*, vol. 1, New Orleans, LA, Oct. 1997, pp. 128–135.

[11] S. Nandi, "Modeling of induction machines including stator and rotor slot effects," *IEEE Transactions on Industry Applications*, vol. 40, no. 4, pp. 1058 – 1065, july-aug. 2004.

[12] M. J. Duran, J. L. Duran, F. Perez, and J. Fernandez, "Induction-motor sensorless vector control with online parameter estimation and overcurrent protection," *IEEE Transactions on Industrial Electronics*, vol. 53, no. 1, pp. 154–161, Dec. 2005.

[13] P. Guglielmi, M. Pastorelli, and A. Vagati, "Cross-saturation effects in IPM motors and related impact on sensorless control," *IEEE Transactions on Industry Applications*, vol. 42, no. 6, pp. 1516 – 1522, nov.-dec. 2006.

[14] N. Bianchi and S. Bolognani, "Influence of rotor geometry of an IPM motor on sensorless control feasibility," *IEEE Transactions on Industry Applications*, vol. 43, no. 1, pp. 87 –96, jan.-feb. 2007.

[15] N. Bianchi and S. Bolognani, "Sensorless–Oriented–Design of PM Motors," *IEEE Transaction on Industry Applications*, vol. 45, no. 4, pp. 1249–1257, Jul./Aug. 2009, "Conf. Rec. of the IEEE 42th Industry Applications Society Annual Meeting, IAS'07", "2007, New Orleans", "23–26 September", "4", "668–675".

[16] S.-C. Yang and R. D. Lorenz, "Comparison of resistance-based and inductance-based self-sensing control for surface permanent magnet machine using high frequency signal injection," in *Energy Conversion Congress and Exposition (ECCE), 2011 IEEE*, sept. 2011, pp. 2701 –2708.

[17] M. Morandin, S. Bolognani, and A. Faggion, "Outer-rotor ringed-pole SPM starter-alternator suited for sensorless drives," in *Symposium on Sensorless Control for Electrical Drives (SLED)*, sept. 2011, pp. 96 –101.

[18] M. Pucci and C. Serporta, "Finite-element Analysis of Rotor Slotting Saliency in Induction Motors for Sensorless Control," *IEEE Transactions on Magnetics*, vol. 46, no. 2, pp. 650–653, Feb. 2010.

[19] J. Melkebeek and J. Willems, "Reciprocity relations for the mutual inductances between orthogonal axis windings in saturated salient-pole machines," *IEEE Transactions on Industry Applications*, vol. 26, no. 1, pp. 107 –114, jan/feb 1990.

[20] N. Limsuwan, T. Kato, C.-Y. Yu, J. Tamura, D. Reigosa, K. Akatsu, and R. D. Lorenz, "Secondary resistive losses with high-frequency injection-based self-sensing in ipm machines," in *Energy Conversion Congress and Exposition (ECCE), 2011 IEEE*, sept. 2011, pp. 622 –629.

[21] S.-C. Yang and R. D. Lorenz, "Analysis of iron and magnet losses in surface permanent magnet machines resulting from injection-based self-sensing position estimation," in *Energy Conversion Congress and Exposition (ECCE), 2011 IEEE*, sept. 2011, pp. 630 –637.

[22] N. Bianchi and S. Bolognani, "Magnetic models of saturated interior permanent magnet motors based on finite element analysis," in *Thirty-Third IAS Annual Meeting. The 1998 IEEE Industry Applications Conference*, vol. 1, oct 1998, pp. 27 –34 vol.1.

[23] J. Walker, D. Dorrell, and C. Cossar, "Flux-linkage calculation in permanent-magnet motors using the frozen permeabilities method," *IEEE Transactions on Magnetics*, vol. 41, no. 10, pp. 3946 – 3948, oct. 2005.

[24] J. K. Tangudu, T. M. Jahns, A. M. El-Refaie, and Z. Q. Zhu, "Segregation of torque components in fractional-slot concentrated-winding interior PM machines using frozen permeability," in *Energy Conversion Congress and Exposition, 2009. ECCE 2009. IEEE*, San Jose, CA, Sep. 2009, pp. 3814–3821.

[25] P. Dular and C. Geuzaine, "GetDP reference manual: the documentation for GetDP, a general environment for the treatment of discrete problems," http://www.geuz.org/getdp/.

[26] J. Gyselinck, P. Dular, N. Sadowski, J. Leite, and J. Bastos, "Incorporation of a Jiles-Atherton vector hysteresis model in 2D FE magnetic field computations: Application of the Newton-Raphson method," *COMPEL: The International Journal for Computation and Mathematics in Electrical and Electronic Engineering*, vol. 23, no. 3, pp. 685–693, 2004.

[27] L. Alberti, M. Barcaro, M. D. Pr, A. Faggion, L. Sgarbossa, N. Bianchi, and S. Bolognani, "IPM machine drive design and tests for an integrated starter–alternator application," *IEEE Transactions on Industry Applications*, vol. 46, no. 3, pp. 993–1001, may-june 2010.

[28] L. Alberti, M. Morandin, N. Bianchi, and S. Bolognani, "Analysis and Tests of the Sensorless Rotor Position Detection of Ringed-Pole PM Motor," in *Symposium on Sensorless Control for Electrical Drives (SLED)*, sept. 2012.

Luigi Alberti (S'07, M'09) received the M.S. degree and the PhD in Electrical Engineering from the University of Padova in 2005 and 2009, respectively. He is currently Researcher at the Faculty of Science and Technology of the Free University of Bozen, Italy, working on design, analysis and control of electric machines and drives, with particular interest in renewable energies and more electric vehicles.

Nicola Bianchi (Verona 1967) received the M.S. and Ph.D. degree in Electrical Engineering from the University of Padova in 1991 and 1995, respectively. Since 1998, he joined the Electric Drives Laboratory at the Department of Electric Engineering of the University of Padova, as a assistant professor. His research activity is in the field of design of electrical motors for electric drive applications.

He is co–author of several papers on the subject of electrical machines and drives, and author of the international text "Electrical Machine Analysis using Finite Elements" CRC Press, Taylor & Francis Group, Boca Raton, and two Italian textbooks.

Mattia Morandin receiver the bachelor degree and the master degree in electronics engineering in 2006 and 2008 respectively, from the University of Padova, Padova, Italy. In 2009 he has been involved in a research activity on hybrid electric vehicles and renewable energy as a scholarship holder. Since 2010, he has been working toward the Ph.D. degree in the analysis and design of synchronous PM motor drives coupled with internal combustion engines for hybrid vehicles, energy generations apparatus and movable electric energy generators.

Johan J. C. Gyselinck received the Master Degree in electrical and mechanical engineering in 1991 and the Doctor of Applied Sciences degree in 2000, both from the Ghent University, Belgium. From 2000 till 2004 he was postdoctoral researcher at the Applied and Computational Electromagnetics (ACE) research Unit of the University of Lige, Belgium. J. Gyselinck is presently associate professor at the Universit Libre de Bruxelles (ULB), Belgium, where he teaches courses on electrical machines and drives and on power electronics. His present research mainly concerns the numerical computation of magnetic fields (mostly using the finite element method), the simulation and control of electrical machines and drives, and renewable energy systems (wind energy and photovoltaics).